Available online at www.sciencedirect.com
SCIENCE DIRECT®
Journal of Solid State Chemistry 177 (2004) 4451–4458
JOURNAL OF SOLID STATE CHEMISTRY
www.elsevier.com/locate/jssc

Temperature dependence of structural parameters in oxide-ion-conducting $Nd_{9.33}(SiO_4)_6O_2$: single crystal X-ray studies from 295 to 900 K

Hiroki Okudera[a,*], Akira Yoshiasa[b,1], Yuuji Masubuchi[c], Mikio Higuchi[c], Shinichi Kikkawa[c]

[a] *Max-Planck-Institut für Festkörperforschung, Heisenbergstraße 1, DE-70569 Stuttgart, Germany*
[b] *Department of Earth and Space Science, Graduate School of Science, Osaka University, 1-1 Machikaneyama-cho, Toyonaka, Osaka 560-0043, Japan*
[c] *Material Science and Engineering, Graduate School of Engineering, Hokkaido University, N13, W8, Kita-ku, Sapporo, Hokkaido 060-8628, Japan*

Received 9 August 2004; received in revised form 17 September 2004; accepted 18 September 2004

Abstract

Crystallographic space group, structural parameters and their thermal changes in oxide-ion-conducting $Nd_{9.33}(SiO_4)_6O_2$ were investigated using high-temperature single-crystal X-ray diffraction experiments in the temperature range of $295 \leqslant T \leqslant 900$ K. The title compound has the apatite structure (space group $P6_3/m$), and no notable structural change occurred over the temperature range examined. Observed anisotropy in thermal motions of oxide ions which belong to SiO_4 tetrahedron indicated high rigidity of the tetrahedron in the structure, indicating that they form *sp*3 hybrid orbitals and the ligand oxygens do not take part in oxide-ion conductivity. Virtually full occupation of the 6*h* Nd site and highly anisotropic displacements of oxide ion inside the hexagonal channel were maintained over the temperature range examined. This result confirms that oxide-ion transport inside the hexagonal channel is the dominant process of conduction in the title compound.

Keywords: Neodymium silicate; Oxide-ion-conductor; Apatite structure type; Thermal vibration; X-ray diffraction; Single crystal structure analysis; High-temperature experiments

1. Introduction

Solid oxide fuel cells are now of great interest as an alternative for internal combustion engines due to their high efficiency and consciousness for natural environment. However, solid electrolyte materials hitherto developed require high operating temperature to attain their high efficiency. For example, operating temperature of yttria stabilized zirconia (YSZ)-utilized fuel cell is in the range 850–1000 °C. It is needless to say that high operating temperature is a potential problem for the construction of the cell and thus safety of the cell in use. From this point of view, oxide-ion-conductive $RE_{9.33}(SiO_4)_6O_2$ (apatite structure; *RE*: rare earth) compounds such as $Nd_{9.33}(SiO_4)_6O_2$ (conductivity $\sigma = 6.3 \times 10^{-3}$ S cm^{-1} with activation energy $E_a = 0.24$ eV at 580 °C [1]) is now of great interest as a new candidate for solid electrolyte materials for a solid oxide fuel cell. By utilizing its excellent transport property at moderate temperatures, more safe and easy-to-handle fuel cells will be realized.

In our previous paper [2], the authors reported that $Nd_{9.33}(SiO_4)_6O_2$ has the apatite prototype structure (space group $P6_3/m$) at 150 K. Highly anisotropic oxide-ion conductivity was ascribed to oxide-ion-transport between adjacent oxide-ion sites arrayed inside the

*Corresponding author. Fax: 49 711 689 1091.
E-mail address: h.okudera@fkf.mpg.de (H. Okudera).
[1] Present address: Department of Earth Sciences, Faculty of Science, Kumamoto University, 2-39-1 Kurokami, Kumamoto 860-8555, Japan.

0022-4596/$ - see front matter © 2004 Elsevier Inc. All rights reserved.
doi:10.1016/j.jssc.2004.09.024

hexagonal channel. Here we show the results of high-temperature X-ray diffraction experiments over the temperature range 295–900 K and discuss the relationship between the structure, thermal displacements of atoms and oxide-ion conductivity.

2. Experimental

2.1. Specimen

Single crystal X-ray diffraction experiments were performed on a $Nd_{9.33}(SiO_4)_6O_2$ crystal synthesized by a floating-zone (FZ) technique. Commercial chemicals of Nd_2O_3 (99.9%) and SiO_2 (99.9%) were used as raw materials and mixed in atomic ratio of Nd:Si = 14:9. Detailed explanations of the sample have been presented in Higuchi et al. [3]. Phase-relationship in the Nd_2O_3–SiO_2 system has been well established by Masubuchi et al. [4,5]. Chemical composition was confirmed by a wavelength dispersive-type electron probe microanalysis (EPMA). The specimens used here were ground into spheres of diameter 0.22 mm. Results of space group determination at 150 K indicated that $P6_3/m$ was most sufficient space group for the present specimens [2].

2.2. Data collection and cell dimension determination

Diffraction intensities and θ angles were measured on two specimens mounted on three four-circle automated diffractometers. One specimen (specimen 1) was fixed at the top of the silica glass fiber of a diameter of 0.1 mm and mounted on a Rigaku AFC-5R diffractometer equipped with N_2 gas-flow temperature control device for intensity data collection (ID) at 295 K (RT1) and cell dimension determinations (CD) at 223 and 295 K. This sample was then moved onto a Rigaku AFC-7R with the same temperature control device for ID at 450 K, CD at 295, 375 and 450 K. The other (specimen 2) was sealed into a silica glass capillary without adhesive and mounted on a Rigaku AFC-5S with air-flow heating device for ID at 295 (RT2), 600, 750 and 900 K, CD at 295 and at every 75 K over the range 375–900 K. Temperature fluctuations were ± 1 K during experiments on AFC-5R and AFC-7R, ± 3 K on AFC-5S at $T \leqslant 750$ K, and ± 5 K on AFC-5S at $T > 750$ K. Intensity data were collected using the ω-2θ scan method [scan width $(1.5 + 0.35\tan\theta)^\circ$ and scan speed 8°/min] with graphite monochromatized Mo $K\alpha$ radiation ($\lambda = 0.71069$ Å). Three standard reflections were monitored at every 200 reflections during the data collection. Around 7000 reflections (including standard reflections) in $2 \times 1/6$ of the reciprocal sphere, with $0 \leqslant h \leqslant 16$, $0 \leqslant k \leqslant 16$, $-13 \leqslant l \leqslant 13$ and their Friedel equivalent reflections, were measured up to $2\theta = 90^\circ$ ($0 \leqslant h \leqslant 17$, $0 \leqslant k \leqslant 17$, $-15 \leqslant l \leqslant 15$ and their Friedel equivalent reflections up to $2\theta = 100^\circ$ at 450 K). The cell dimensions were determined with θ values of the 24 most intense reflections in the 2θ range of 54–70° measured by the half-shutter method. Observed θ values were calibrated with those for Si single crystal. Experimental conditions are listed in Table 1. Changes in the cell dimensions with temperature are shown in Fig. 1. Observed cell dimensions are also shown in Table 2 for selected temperatures.

Table 1
Crystal data and details of data collection for $Nd_{9.33}(SiO_4)_6O_2$

Crystal data	
Chemical formula	$Nd_{9.33}(SiO_4)_6O_2$
Chemical formula weight	1930
Space group	$P6_3/m$
Z	1
$F_{(000)}$	852
Radiation type	Mo$K\alpha$
Wavelength (Å)	0.71069
No. of reflections for cell parameters	24
2θ range (°)	54–70
Crystal form, color	Sphere, purple
Crystal radius (mm)	0.11
μ(mm^{-1})	21.8 (RT1)
Data collection	
Specimen 1	
Temperature control	N_2 gas flow
Fluctuation (K)	± 1
Diffractometer	Rigaku AFC-5R
Temperature (K)	
Structure refinement	295 (RT1)
Cell dimensions	223, 295
Diffractometer	Rigaku AFC-7R
Temperature (K)	
Structure refinement	450
Cell dimensions	293, 375, 450
Specimen 2	
Temperature control	Air flow
Fluctuation (K)	± 3 at $T \leqslant 750$ K, ± 5 at $T > 750$ K
Diffractometer	Rigaku AFC-5S
Temperature (K)	
Structure refinement	295 (RT2), 600, 750, 900
Cell dimensions	295, 375, 450, 525, 600, 675, 750, 825, 900
2θ range (°)	$\leqslant 90$ ($2\theta \leqslant 100$ at 450 K)
Scan method and width (°)	$\omega/2\theta$ scan, $1.5 + 0.35\tan\theta$
Range of h, k, l	$0 \leqslant h \leqslant 16$, $0 \leqslant k \leqslant 16$, $-13 \leqslant l \leqslant 13$ ($0 \leqslant h \leqslant 17$, $0 \leqslant k \leqslant 17$, $-15 \leqslant l \leqslant 15$ at 450 K) and their Friedel equivalent reflections
No. of standard reflections	3
Frequency of standard reflections	Every 200 data
Minimum and maximum Intensity fluctuation (%) [a]	1.6 (RT2), 8.4 (900 K) [a]

[a] $\{[F_{obs}\}_{max} - \{F_{obs}\}_{min}\}/|F_{obs}|_{min}$ 5 −4 8 reflection. See text for equation.

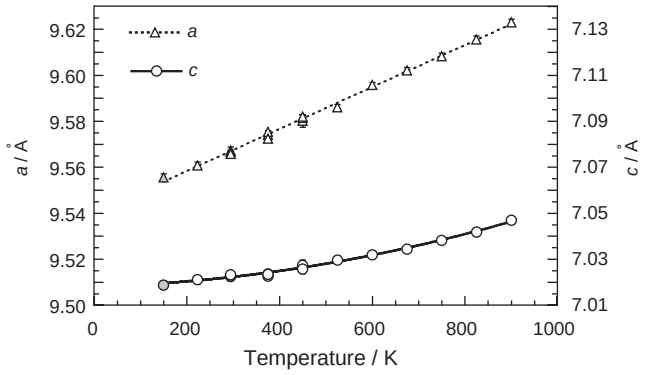

Fig. 1. Temperature variation of the cell dimensions between 150 and 900 K. Open triangles: a length; open circles: c length. The 150 K data taken from Okudera et al. [2] are shown with hatched symbols. Error bars (1σ) are hidden behind the symbols. The dashed and solid lines correspond to Eqs. (1) and (2), respectively.

2.3. Crystal structure refinement

The intensity data were corrected for Lp and absorption ($\mu R = 2.39$ at RT1) factors. Observed structure amplitudes were then simply averaged for equivalent ones, and two data criteria were applied at this stage. One was commonly used $|\bar{F}_{obs}| > 3\sigma(|\bar{F}_{obs}|)$ and the other was $\{|F_{obs}|_{max} - |F_{obs}|_{min}\}/|F_{obs}|_{min} < R_{tr}$ [2,6]. In this study we set $R_{tr} = 0.10$, and $|\bar{F}_{obs}|$s which obeyed these two criteria were used in the structure refinements with weight of $1/\sigma^2(|\bar{F}_{obs}|)$. The numbers of independent reflections used for refinements are given in Table 2. The least-squares program ORXFLS4, the 1977 version of ORFLS [7] was used for refinements with variables including one scale and one isotropic extinction factor (type I of Coppens and Hamilton [8]). The neutral form factors and anomalous dispersion terms were taken from International Tables for Crystallography vol. C. $M1$ and $M2$ sites were assumed to be occupied by Nd and the total number of Nd atoms was fixed at 9.33 in a cell. The other sites were assumed to be fully occupied except as noted. Residual electron densities were calculated with computation of the difference Fourier syntheses after convergence of least-squares calculations.

3. Results

3.1. Thermal change in cell dimensions

Observed cell dimensions were fitted using a linear equation for a and a second-order polynomial for c together with the 150 K data [2]. These two equations were used to obtain the solid and dashed lines in Fig. 1:

$$a\,(\text{Å}) = 9.540 + 9.127 \times 10^{-5} T, \quad (1)$$

$$c\,(\text{Å}) = 7.018 + 5.359 \times 10^{-6} T + 2.892 \times 10^{-8} T^2, \quad (2)$$

where T is absolute temperature. The square of the multiple correlation coefficients, R^2, are 99.9% and 99.6% for Eqs. (1) and (2), respectively. Observed thermal expansion of the cell was anisotropic and dominant along the a-axis: at 900 K the a and c values were 100.7% and 100.4%, respectively, of those at 150 K.

3.2. Crystal structure

Prior to the structure refinement with the apatite structure, that is the structure at 150 K, possibility of $P\bar{3}$ space group was examined by the same procedure applied for the 150 K data [2]; $P6_3/m$ was most sufficient space group for the present specimens over the temperature range examined. Detailed examinations of the O1–O3 site positions are presented later in this section.

Distribution of oxide ions inside the hexagonal channel was examined in the following way. First, structural parameters were refined in the apatite structure (O4 site at $2a$ position: 0,0,1/4) with anisotropic atomic displacement parameters (ADPs) for all atomic sites (anisotropic $2a$ model; 41 parameters). These refinements converged at wR ranging from 0.022 to 0.027 for the two specimens. After the convergence, further structure refinements were made in two ways. One was that the O4 site was split into two positions (at $4e$ position: 0,0,z) on the c-axis and the other was that the O4 site was split into three (at both $2a$ and $4e$ positions). Total number of oxide ions inside the hexagonal channel was fixed at two in a cell. Among these structure refinements, only the calculation with isotropic ADP for the O4 site at $4e$ position (isotropic $4e$ model; 41 parameters) converged successfully with the O4 site position $z \approx 0.22$. There was no notable difference in wR values between these two models. It means that both anisotropic $2a$ and isotropic $4e$ models yielded good fits. However, comparisons of residual density maps indicated that the refinements with anisotropic $2a$ model yielded a better fit in view of electron density distribution inside the hexagonal channel. Moreover, there was no negative hole at the O4 site position ($z = 1/4$) after anisotropic $2a$ refinement. This result clearly indicates that unimodal and highly anisotropic function around the $2a$ position is still the best description of probability density function of oxide ion in the hexagonal channel. Note that the refined z value in the isotropic $4e$ model was a calculational artifact to fit actual electron density distribution by spherically symmetric ones. While possibility of site-splitting of O4 site might be still remaining, their separation, if any, is smaller than the experimental resolution or simply very ambiguous. Full occupation of the O4 site was confirmed within an esd at all temperatures by further iterations of least-squares cycles

Table 2
Results of least-squares calculations, structure parameters and atomic displacement parameters (Å^2) of $Nd_{9.33}(SiO_4)_6O_2$ at various temperatures

		295 K (RT1)	295 K (RT2)	450 K	600 K	750 K	900 K
	a (Å)	9.567(2)	9.566(1)	9.5820(9)	9.596(1)	9.608(1)	9.623(1)
	c (Å)	7.023(2)	7.023(1)	7.0257(9)	7.032(1)	7.038(2)	7.047(2)
	Ext. [a]	0.32(1)	0.43(1)	0.38(1)	0.41(1)	0.41(1)	0.38(1)
*M*1 4*f* 3	occ. [b]	0.857(2)	0.853(2)	0.854(1)	0.855(2)	0.853(2)	0.852(2)
Nd	x	2/3	2/3	2/3	2/3	2/3	2/3
	y	1/3	1/3	1/3	1/3	1/3	1/3
	z	0.0008(1)	0.00107(7)	0.00093(7)	0.00040(9)	0.0003(1)	0.0001(1)
	$u_{(11)}$	0.0095(1)	0.00870(9)	0.01179(8)	0.0147(1)	0.0176(2)	0.0209(2)
	$u_{(33)}$	0.0215(3)	0.0202(2)	0.0224(2)	0.0241(3)	0.0257(3)	0.0277(3)
*M*2 6*h m*	occ. [b]	0.984	0.986	0.985	0.985	0.987	0.988
Nd	x	0.01040(4)	0.01041(3)	0.01036(3)	0.01033(4)	0.01037(4)	0.01044(5)
	y	0.23995(4)	0.24012(3)	0.23968(3)	0.23929(4)	0.23905(4)	0.23898(5)
	z	1/4	1/4	1/4	1/4	1/4	1/4
	$u_{(11)}$	0.0074(1)	0.00669(9)	0.00966(8)	0.0120(1)	0.0144(2)	0.0176(2)
	$u_{(22)}$	0.0088(1)	0.00828(9)	0.01139(8)	0.0140(1)	0.0167(2)	0.0200(2)
	$u_{(33)}$	0.0087(1)	0.00804(9)	0.01101(8)	0.0134(1)	0.0160(1)	0.0188(2)
	$u_{(12)}$	0.0028(1)	0.00262(7)	0.00404(6)	0.00502(9)	0.0062(1)	0.0077(1)
*M*3 6*h m*	x	0.4013(2)	0.4016(2)	0.4014(1)	0.4017(2)	0.4016(2)	0.4012(2)
Si	y	0.3722(2)	0.3723(2)	0.3725(1)	0.3728(2)	0.3730(2)	0.3729(2)
	z	1/4	1/4	1/4	1/4	1/4	1/4
	$u_{(11)}$	0.0087(7)	0.0085(4)	0.0104(4)	0.0125(5)	0.0138(7)	0.0166(8)
	$u_{(22)}$	0.0074(7)	0.0073(4)	0.0092(4)	0.0111(5)	0.0128(6)	0.0143(7)
	$u_{(33)}$	0.0073(7)	0.0067(4)	0.0092(4)	0.0110(6)	0.0127(7)	0.0149(7)
	$u_{(12)}$	0.0047(5)	0.0050(4)	0.0060(3)	0.0069(5)	0.0078(6)	0.0088(6)
O1 6*h m*	x	0.3223(9)	0.3229(6)	0.3227(6)	0.3230(8)	0.3230(9)	0.322(1)
O	y	0.4866(8)	0.4875(6)	0.4869(6)	0.4876(7)	0.4870(9)	0.487(1)
	z	1/4	1/4	1/4	1/4	1/4	1/4
	$u_{(11)}$	0.039(3)	0.031(2)	0.036(2)	0.041(3)	0.046(4)	0.051(4)
	$u_{(22)}$	0.032(3)	0.025(2)	0.028(2)	0.035(2)	0.035(3)	0.041(3)
	$u_{(33)}$	0.016(2)	0.017(2)	0.021(2)	0.019(2)	0.027(3)	0.035(4)
	$u_{(12)}$	0.033(3)	0.025(2)	0.028(2)	0.034(2)	0.034(3)	0.039(3)
O2 6*h m*	x	0.5267(6)	0.5265(5)	0.5274(5)	0.5269(6)	0.5276(7)	0.5274(7)
O	y	0.1238(7)	0.1239(5)	0.1243(5)	0.1226(7)	0.1230(7)	0.1234(7)
	z	1/4	1/4	1/4	1/4	1/4	1/4
	$u_{(11)}$	0.012(2)	0.009(1)	0.015(1)	0.017(2)	0.017(2)	0.020(2)
	$u_{(22)}$	0.015(2)	0.015(1)	0.018(1)	0.023(2)	0.024(2)	0.026(3)
	$u_{(33)}$	0.024(3)	0.022(2)	0.029(2)	0.033(3)	0.036(3)	0.042(4)
	$u_{(12)}$	0.006(2)	0.006(1)	0.010(1)	0.013(2)	0.013(2)	0.015(2)
O3 12*i* 1	x	0.3459(7)	0.3469(6)	0.3462(6)	0.3450(7)	0.3451(7)	0.3448(8)
O	y	0.2540(5)	0.2542(4)	0.2545(4)	0.2546(5)	0.2547(5)	0.2550(6)
	z	0.0664(7)	0.0647(5)	0.0650(5)	0.0658(7)	0.0669(7)	0.0674(7)
	$u_{(11)}$	0.055(3)	0.049(2)	0.059(2)	0.066(3)	0.069(3)	0.076(4)
	$u_{(22)}$	0.019(2)	0.019(1)	0.021(1)	0.025(2)	0.028(2)	0.031(2)
	$u_{(33)}$	0.015(2)	0.011(1)	0.013(1)	0.020(2)	0.019(2)	0.022(2)
	$u_{(12)}$	0.023(2)	0.020(1)	0.022(1)	0.027(2)	0.028(2)	0.030(2)
	$u_{(13)}$	−0.019(2)	−0.016(1)	−0.016(1)	−0.021(2)	−0.021(2)	−0.023(3)
	$u_{(23)}$	−0.009(2)	−0.007(1)	−0.006(1)	−0.009(1)	−0.009(2)	−0.008(2)
O4 2*a* $\bar{6}$	x	0	0	0	0	0	0
O	y	0	0	0	0	0	0
	z	1/4	1/4	1/4	1/4	1/4	1/4
	$u_{(11)}$	0.015(2)	0.014(2)	0.019(2)	0.025(2)	0.023(2)	0.032(3)
	$u_{(33)}$	0.07(1)	0.068(9)	0.080(9)	0.09(1)	0.12(2)	0.11(2)
N_{meas} [c]		6970	6978	8808*	6997	7010	7056
N_{ind} [d]		1623	1621	2058	1632	1640	1644
R_{int} (%) [e]		5.96	2.81	3.16	4.75	5.40	6.05
N_{used} [f]		560	870	1020	631	579	505
$R_{int.used}$ (%) [g]		1.38	1.23	1.23	1.30	1.32	1.37
R (%)		1.77	1.82	2.01	1.64	1.79	1.81

Table 2 (*continued*)

	295 K (RT1)	295 K (RT2)	450 K	600 K	750 K	900 K
wR (%)	2.13	2.42	2.69	2.08	2.24	2.21
S	0.67	0.87	0.96	0.70	0.74	0.73
D_{max} (e/Å^3) [h]	1.07	2.82	3.51	1.49	1.24	1.30
D_{min} (e/Å^3) [i]	−0.98	−1.35	−1.63	−1.01	−1.16	−1.05

*2θ up to 100° at 450 K.

[a]Isotropic extinction factor for type I extinction.

[b]Site occupancy parameter.

[c]Total number of measured reflections.

[d]Number of independent reflections.

[e]Internal consistency among reflections obeying $|\bar{F}_{obs}| > 3\sigma(|\bar{F}_{obs}|)$ criterion.

[f]Number of independent reflections used in structure refinements.

[g]Internal consistency among reflections used in structure refinements.

[h]Maximum residual after structure refinement.

[i]Minimum residual after structure refinement. Anisotropic thermal parameters were refined in the form:

$$T = \exp[-2\pi^2(u_{(11)}a^{*2}h^2 + u_{(22)}b^{*2}k^2 + u_{(33)}c^{*2}l^2 + 2u_{(12)}a^*b^*hk + 2u_{(13)}a^*c^*hl + 2u_{(23)}b^*c^*kl)].$$

The site symmetries give the constraints: $u_{(11)} = u_{(22)} = 2\,u_{(12)}$, $u_{(13)} = u_{(23)} = 0$ at $M1$ and O4 sites; $u_{(13)} = u_{(23)} = 0$ at $M2$, $M3$, O1 and O2 sites. Only independent thermal parameters are shown. Esds (1σ) are in parentheses.

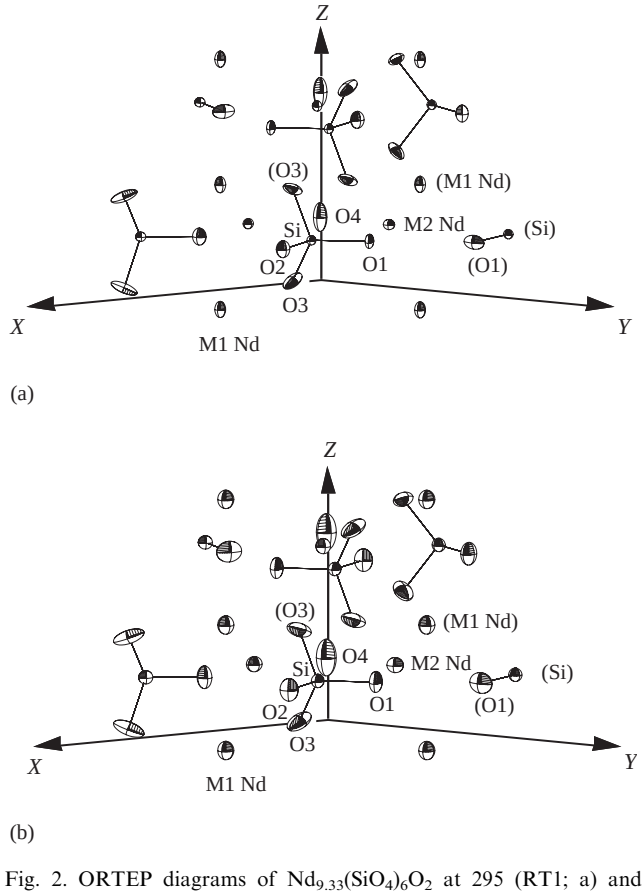

Fig. 2. ORTEP diagrams of $Nd_{9.33}(SiO_4)_6O_2$ at 295 (RT1; a) and 900 K (b). Thermal vibrational ellipsoids represent 50% of probability. Atoms in the region $-0.5 \leqslant x \leqslant 6.3$, $-0.5 \leqslant y \leqslant 6.3$, $-0.01 \leqslant z \leqslant 7.3$ (Å) are plotted. Atoms in the asymmetric unit and some of their equivalents are labeled without and with brackets, respectively.

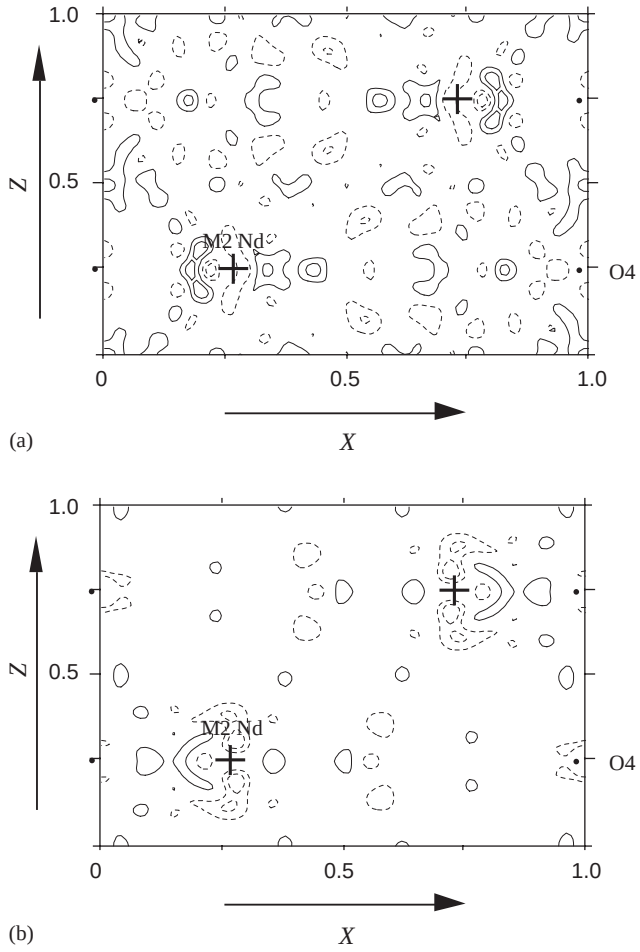

Fig. 3. Difference Fourier maps of $Nd_{9.33}(SiO_4)_6O_2$ at 295 K (RT1; a) and 900 K (b) in XZ plane ($y = 0$). Contours: −0.667, −0.333, 0.333, 0.667 eÅ^{-3}. Solid and dashed lines are positive and negative contours, respectively. Zero contours omitted.

Table 3
Selected interatomic distances, angles and polyhedral volumes

Bond	Distances (Å), angles (°) and polyhedral volumes (Å^3)					
	295 K (RT1)	295 K (RT2)	450 K	600 K	750 K	900 K
M1 site						
Nd–O1 [× 3]	2.429(4)	2.426(3)	2.431(3)	2.427(6)	2.433(4)	2.436(5)
Nd–O2 [× 3]	2.488(4)	2.487(3)	2.486(3)	2.501(6)	2.501(4)	2.504(5)
Nd–O3 [× 3]	2.806(5)	2.796(4)	2.808(4)	2.825(5)	2.829(5)	2.837(6)
Mean value	2.574(4)	2.569(3)	2.575(3)	2.584(6)	2.588(5)	2.592(5)
Polyhedral volume	32.73(7)	32.62(6)	32.78(5)	33.10(7)	33.23(8)	33.38(9)
M2 site						
Nd–O1	2.726(6)	2.731(5)	2.735(5)	2.744(5)	2.746(6)	2.746(7)
Nd–O2	2.466(5)	2.447(4)	2.478(4)	2.481(5)	2.492(6)	2.495(6)
Nd–O3 [× 2]	2.547(4)	2.553(3)	2.558(3)	2.559(4)	2.559(4)	2.564(5)
Nd–O3′ [× 2]	2.405(5)	2.396(4)	2.398(4)	2.402(5)	2.413(5)	2.418(5)
Nd–O4	2.2475(4)	2.2488(4)	2.2486(4)	2.2482(5)	2.2487(5)	2.2512(6)
Mean value	2.477(4)	2.475(3)	2.482(3)	2.485(4)	2.490(4)	2.494(5)
Polyhedral volume	22.32(6)	22.22(4)	22.43(4)	22.54(5)	22.66(6)	22.75(6)
M3 site						
Si–O1	1.61(1)	1.616(8)	1.612(8)	1.618(9)	1.61(1)	1.61(1)
Si–O2	1.623(2)	1.638(1)	1.622(1)	1.612(2)	1.613(2)	1.624(2)
Si–O3 [× 2]	1.619(5)	1.629(4)	1.628(4)	1.626(5)	1.622(5)	1.619(5)
Mean value	1.618(5)	1.628(4)	1.622(4)	1.621(5)	1.617(5)	1.619(6)
O1–Si–O2	112.9(3)	112.4(3)	113.1(2)	112.7(3)	113.1(3)	113.2(4)
O1–Si–O3 [× 2]	111.9(3)	112.1(2)	111.8(2)	111.6(3)	111.7(3)	111.7(4)
O2–Si–O3 [× 2]	107.1(3)	106.9(2)	106.8(2)	107.5(3)	107.3(3)	107.3(3)
O3–Si–O3	105.5(2)	106.1(2)	106.0(2)	105.6(2)	105.3(2)	105.3(3)
Polyhedral volume	2.17(1)	2.206(9)	2.183(8)	2.18(1)	2.16(1)	2.17(1)

with site occupancy factor (SOF) of the O4 site as one of refinable parameters.

Positions of the other oxide ion sites were checked again by difference Fourier syntheses after anisotropic 2*a* refinements. Detailed investigations of residual density maps in the vicinity of O1 and O3 site positions showed weak positive residues at these positions and shallow negative holes on their first principal axes. This result leads us to the same conclusion made for the O4 site position also for these positions; unimodal and anisotropic displacements of atoms is the best explanation of observed electron density distributions. On the other hand, there was virtually no residual density around the O2 site position. In consequence, there was no deviation from the apatite structure on the present samples over the temperature range examined. Results of least-squares calculations with anisotropic 2*a* model and parameter values at various temperatures are presented in Table 2. ORTEP diagrams and residual electron density maps at several temperatures are shown in Figs. 2 and 3, respectively.

Further iterations were made with SOFs of cations as refinable parameters. No constraint was applied for the atomic ratio of Nd and Si in these calculations. These iterations yielded ~1% smaller SOFs of cations than those in Table 2 with virtually the same *R*-values. This result is quite reasonable since neutral form factors are applied for atoms having ionic character. Even in these calculations, Nd–Si ratio was 9.33:6 within esd at all temperatures.

3.3. Interatomic distances and atomic displacements

The thermal changes of selected interatomic distances, polyhedral volumes and O–Si–O angles are presented in Table 3. Thermal changes in Nd–O distances showed increasing trends, while there were some variations even among two room temperature values. Observed Si–O distances were virtually constant in the temperature range examined, and O–Si–O angles were close to the value for regular tetrahedron (≈109°). Observed mean square displacements (m.s.d. 's, $\langle u^2 \rangle$) along principal axes of thermal vibrational ellipsoids steadily increased with temperature at all atomic sites. Directions of principal axes and relationships among $\langle u^2 \rangle$'s along these directions were maintained in the temperature range examined. Thermal changes in U_{equiv} and anisotropy in $\langle u^2 \rangle$'s are shown in Fig. 4 for selected atomic sites. As can be seen in Fig. 4b, anisotropy steadily decreased at *M*1–*M*3 sites with increasing temperature. It was hard to define thermal trends in anisotropy of thermal displacements of oxide ions, but highest anisotropy was found at O3 site, not the O4 site where high anisotropy was expected for oxide-ion conductivity.

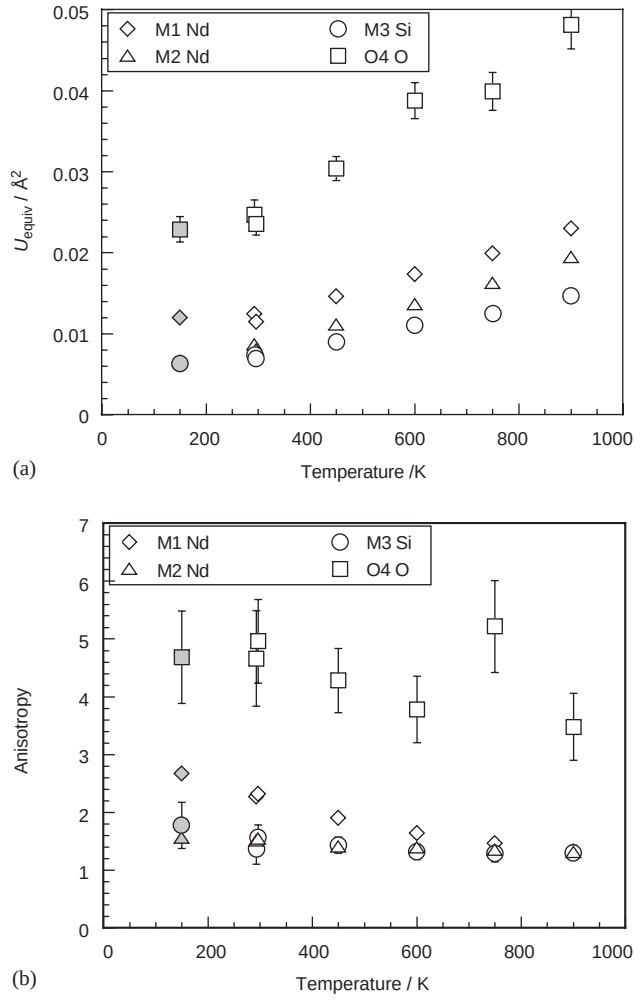

Fig. 4. Changes in isotropic displacement parameter, U_{equiv} (a), and anisotropy in $\langle u^2 \rangle$'s (b) at selected atomic sites, along the principal axes of their thermal vibrational ellipsoids. The values plotted in (b) show $\langle u^2 \rangle_{max}/\langle u^2 \rangle_{min}$, where $\langle u^2 \rangle_{max}$ and $\langle u^2 \rangle_{min}$ are maximum and minimum $\langle u^2 \rangle$ values at the site. Error bars (1σ) are hidden behind symbols at some data points. Open diamonds: *M*1 site (Nd); open triangles: *M*2 site (Nd); open circles: *M*3 site (Si); open squares: O4 site. RT values are shifted for clarity. The 150 K data taken from Okudera et al. [2] are shown with hatched symbols.

4. Discussion

4.1. Interstitial oxide ion site

Recent theoretical and experimental studies on $La_{9.33}(SiO_4)_6O_2$ [9,10] commonly suggested presence of two interstitial oxide ions between M2 site positions array in the *c*-axis direction (e.g. at 0.0135, 0.2333, 0.8763 [9]). However, there was no condensation of positive residues in the corresponding region (Fig. 3). Maxima of residuals (Table 2) were commonly found in the vicinity of Nd atoms (0.46–0.63 Å apart from Nd sites), and there was no sign of interstitial oxide ion in the structure. Observed positive and negative densities in the vicinity of *M*2 site position (Fig. 3) might be attributable to anharmonic thermal motions of Nd atoms.

4.2. Rigidity of SiO_4 tetrahedron

In our previous study, the authors pointed out the high rigidity of SiO_4 tetrahedron. Here we confirm this also at high temperatures because high rigidity, in other words formation of *sp*3 hybrid orbital among these atoms, certifies no contribution of these ligand oxygens on oxide-ion conductivity. As it is pointed out in Section 3.3, Si–O distances were virtually constant in spite of different temperatures. In addition, comparisons of $\langle u^2 \rangle$'s of Si and ligand oxygens along their bonds showed that these values were rather close to each other when their esds were taken into consideration. These are features expected from librational motion of the SiO_4 tetrahedron around the Si atom. Even though differences among O–Si–O angles (up to 6–8°) indicated a certain amount of distortion, SiO_4 tetrahedron existed as a rather rigid unit in the structure. This rigidity suggest no contribution of O1–O3 site oxide ions to oxide-ion conduction. Thermal vibrational ellipsoids at O1 and O3 sites were highly elongated in particular directions (Fig. 2), not oblate ellipsoidal as expected for a tetrahedron librating in a free space. From atomic bonding point of view, O3 site lies at the center of a face of triangle pyramid formed by its neighboring cations, and thermal displacements of O3 site oxide ion are dominant in the direction normal to the face. The same consideration is possible for O1 site, but O2 site is coordinated by four cations and thermal displacements of O2 site oxide ion are more isotropic than the other oxide ions.

4.3. Distribution of O4 site oxide ion and oxide-ion conductivity

At 150 K the cation vacancy was preferably located at the *M*1 site, and the *M*2 site (the other Nd site) was essentially fully occupied [2]. This full occupation of *M*2 site was maintained even at 900 K (Table 2). In addition, as it is discussed above, probability density distribution of O4 site oxide ion was still highly anisotropic and elongated in the *c*-axis direction. This result indicates that smooth potential wave inside the hexagonal channel is maintained at high temperatures, and oxide-ion transport inside the channel is a cause of anisotropically high conductivity along the *c*-axis direction in the subjected compound. While Nakayama et al. [11] reported inflection point on thermal change in conductivity at around 600 K, we could not find any apparent difference on structures below and above the temperature. The cause of this inflection point is still an open question.

References

[1] Y. Masubuchi, M. Higuchi, H. Katase, T. Takeda, S. Kikkawa, K. Kodaira, S. Nakayama, Solid State Ion. 166 (2004) 213–217.
[2] H. Okudera, Y. Masubuchi, S. Kikkawa, A. Yoshiasa, Z. Kristallogr. 219 (2004) 27–31.
[3] M. Higuchi, K. Kodaira, S. Nakayama, J. Crystal Growth 207 (1999) 298–302.
[4] Y. Masubuchi, M. Higuchi, K. Kodaira, J. Crystal Growth 247 (2003) 207–212.
[5] Y. Masubuchi, M. Higuchi, H. Katase, T. Takeda, S. Kikkawa, K. Kodaira, S. Nakayama, Solid State Ion. 166 (2004) 213–217.
[6] H. Okudera, Proceedings of the Eighth International Conference on Ferrite, Kyoto, August 2000, 2001, pp. 293–294.
[7] W.R. Busing, K.O. Martin, H.A. Levy, ORFLS, Report ORNL-TM-305, Oak Ridge National Laboratory, Oak Ridge, TN, USA, 1962.
[8] P. Coppens, W.S. Hamilton, Acta Crystallogr. A 26 (1970) 71–83.
[9] J.R. Tolchard, M.S. Islam, P.R. Slater, J. Mater. Chem. 13 (2003) 1956–1961.
[10] L. León-Reina, E.R. Losilla, M. Martínez-Lara, S. Bruque, M.A.G. Aranda, J. Mater. Chem. 14 (2004) 1142–1149.
[11] S. Nakayama, M. Sakamoto, M. Higuchi, K. Kodaira, M. Sato, S. Kakita, T. Suzuki, K. Itoh, J. Eur. Ceram. Soc. 19 (1999) 507–510.